

Investigation of laser direct energy deposition for production of ODS alloys

**Nuclear Technology
Research and Development**

***Prepared for
U.S. Department of Energy
Nuclear Technology R&D
Advanced Fuels Campaign***

***N. Sridharan, S. Dryepondt, and K.G. Field
Oak Ridge National Laboratory***

***September 2018
M3NT-18OR020202072***



DISCLAIMER

This information was prepared as an account of work sponsored by an agency of the U.S. Government. Neither the U.S. Government nor any agency thereof, nor any of their employees, makes any warranty, expressed or implied, or assumes any legal liability or responsibility for the accuracy, completeness, or usefulness, of any information, apparatus, product, or process disclosed, or represents that its use would not infringe privately owned rights. References herein to any specific commercial product, process, or service by trade name, trade mark, manufacturer, or otherwise, does not necessarily constitute or imply its endorsement, recommendation, or favoring by the U.S. Government or any agency thereof. The views and opinions of authors expressed herein do not necessarily state or reflect those of the U.S. Government or any agency thereof.

SUMMARY

Laser blown powder additive manufacturing (AM) was performed to evaluate the feasibility of using the technique to fabricate oxide dispersion strengthened (ODS) alloys. The idea was to utilize an in-situ oxidation reaction to oxidize reactive elements to generate a refined dispersion of the dispersoids with a uniform size distribution. Builds were fabricated using Y added 316L in a reactive atmosphere and an inert atmosphere for comparisons. Detailed characterization was performed to understand the as-fabricated microstructure. Detailed characterization and chemical analysis show that there is significant Y loss during deposition. The loss in Y during processing leads to a reduced volume fraction of precipitates ($\sim 2 \times 10^{18}/\text{m}^3$) with an average size of ~ 97 nm. Mechanical testing of the samples fabricated in both air and in inert atmosphere were performed at RT, 200°C, 400°C and 600°C. The mechanical properties were then compared with austenitic ODS alloys that were reported in the literature. The results show that while the ultimate tensile strengths were comparable with wrought ODS alloys, the deterioration in yield strength with temperature was more severe in the case of the AM fabricated ODS material. However, the ductility was observed to be higher than all wrought 316L ODS alloys. Future efforts will focus on increasing the percentage of Y in the pre-alloyed powder to refine the dispersoids. In addition, a close control of process parameters and post processing treatments need to be explored to optimize the dispersoids volume fraction.

CONTENTS

SUMMARY	iii
ACRONYMS.....	viii
1. INTRODUCTION.....	1
2. EXPERIMENTAL PROCEDURE	2
3. RESULTS AND DISCUSSION	3
3.1 Microstructure characterization	3
3.1.1 As-received powder	3
3.1.2 As-fabricated structure.....	4
3.1.3 Mechanical behavior.....	7
4. SUMMARY AND CONCLUSIONS.....	9
5. REFERENCES.....	10

FIGURES

Figure 1: Schematic illustration of the fabrication of wrought ODS alloys using conventional approach [8] and the proposed approach to fabricate ODS alloys.	1
Figure 2: (a) Micrograph showing the structure and the presence of dispersoids in the as-fabricated powder (b) Figure 2(a) in higher magnification	3
Figure 3: (a) Dispersoids (black contrast) embedded in the matrix and inset showing a magnified region in Figure 3(a). (b) Particle size distribution measured using ImageJ showing a peak at 30 nm with an average size of 97 nm.	5
Figure 4: (a) Inverse pole figure (IPF) of the sample fabricated under atmosphere (b) Higher magnification IPF of the region marked in (a) (c) Phase map corresponding to (b) clearly showing the presence of δ ferrite formed as a consequence of solidification (d) Shows that δ -ferrite has an orientation relationship with the austenite phase	5
Figure 5: Structure of the as-fabricated sample (a) micrograph of the sample showing the presence of oxide nano-dispersoids (b) Histogram showing the size distribution of the oxide particles in the as-fabricated structure (c) Comparison between the size distributions of the samples fabricated in air and Ar (d) Showing the differences in N, O and Y between the two samples.	6
Figure 6: (a) Inverse pole figure (IPF) of the sample fabricated under Ar (b) Higher magnification IPF of the region marked in (a) (c) Phase map corresponding to (b) clearly showing the presence of δ ferrite formed as a consequence of solidification (d) Shows that δ -ferrite has an orientation relationship with the austenite phase	7
Figure 7: Engineering stress strain curves for the samples fabricated in air and in Ar.	8
Figure 8: Comparison between the mechanical properties as a function of temperature for the AM ODS alloys vs wrought alloys [31]–[34].....	8

Figure 9: Inverse pole figure performed on the heads of the deformed specimens deformed at (a) RT (b) 200°C (c) 400°C and (d) 600°C note the decrease in the number of twins with increase in the deformation temperature.9

TABLES

Table 1: Composition of the as received powder in weight percent.....3
Table 2: Composition of the fabricated builds in weight percent.....4

ACRONYMS

AM	Additive manufacturing
Ar	Argon
BCC	Body centered cubic
DED	Direct energy deposition
EBSD	Electron back scatter diffraction
FA	Ferrite-Austenite
FCC	Face centered cubic
FEG	Field emission gun
GARS	Gas atomization reactive synthesis
HIP	Hot isostatic pressing
N	Nitrogen
nm	nanometer
O	Oxygen
ODS	Oxide dispersion strengthened
SiO ₂	Silicon dioxide
SLM	Selective laser melting
SEM	Scanning electron microscopy
TEM	Transmission electron microscopy
UTS	Ultimate tensile strength
Y	Yttrium
YS	Yield stress
μm	micrometer

INVESTIGATION OF LASER DIRECT ENERGY DEPOSITION FOR PRODUCTION OF ODS ALLOYS

1. INTRODUCTION

The next generation of nuclear reactors will require materials to maintain their performance in extreme environments such as elevated temperature, aggressive coolants, and intense neutron flux [1]. Few materials are available which could potentially withstand such aggressive conditions. One candidate material class is oxide dispersion strengthened (ODS) alloys [2], [3]. ODS alloys have a fine dispersion of nanometer sized oxide clusters/particles embedded in a ferritic or austenitic matrix. The nanoclusters retard grain growth at elevated temperatures and serve to pin the dislocations, thus improving strength even at elevated temperatures [2], [4]–[6]. In addition, the cluster-matrix interfaces also serve to absorb point defects generated during irradiation, thus reducing radiation-induced swelling [2]. The fundamental reason for this impressive behavior is still under investigation [2] [6]. However, it is generally agreed upon that the steel derives this strength from the fine dispersion of oxide nano-clusters [4], [5]. Despite their significant benefits, the widespread adoption of these advanced ODS alloys is limited [7]. Manufacturing challenges are the most crucial factor which limit the application of advanced materials in advanced nuclear reactors. At present, the production of most ODS alloy variants involve a series of processing steps including ball milling/mechanical alloying, powder consolidation by extrusion or hot isostatic pressing (HIP), and tube fabrication by hot/cold pilgering. Ball milling is a key step because it leads to a supersaturation of Y and O in the ferritic matrix that can react and form very fine nano-clusters upon heating. A schematic of the production of wrought ODS alloys is shown in Figure 1.

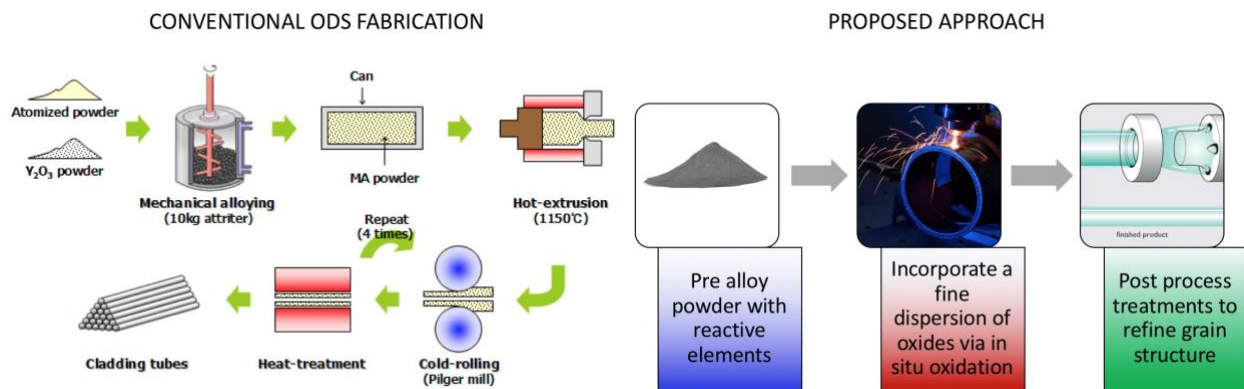


Figure 1: Schematic illustration of the fabrication of wrought ODS alloys using conventional approach [8] and the proposed approach to fabricate ODS alloys.

However, by leveraging advanced manufacturing processes it may be possible to reduce the number of processing steps from four or more to as little as two steps. The advent of AM, which is capable of precise process control in a localized manner, may enable the production of ODS alloy variants with site-specific cluster dispersions and the incorporation of nanoclusters in-situ during the melting/solidification or consolidation processes. One could leverage two different approaches to generate these oxides in-situ. One approach is to use the concept of “solute trapping” where the reactive metal is trapped in the matrix as a result of high liquid solid interface velocities promoted by high solidification rates [9]. The trapped oxygen and reactive elements then form an oxide dispersion upon further heat treatment. This approach was previously implemented by Rieken et al. who synthesized powders using GARS (Gas Atomization Reactive Synthesis) and consolidated the powders using HIP [10]–[12]. The powders would contain the reactive

elements in solid solution, and gas atomization was conducted in a well-controlled oxidizing atmosphere to form a very fine Chromia layer at the powder particle surface. Upon HIP'ing, the reactive elements would react with O due to their high affinity for oxygen and form the desired nanoclusters [10], [11].

Boegelein et al. have used selective laser melting (SLM) to fabricate ODS Fe-20Cr-5Al-Y alloys using ball milled PM2000 powder [13], [14]. They reported that upon post-weld annealing a fine dispersion of Y-rich precipitates were observed by transmission electron microscopy (TEM) [13], [14]. However, one of the primary challenges in the fabrication of SLM ODS alloys using ball milled powder is the formation of Y-rich slag during processing. The formation of slag is promoted because of the differences in density between Ytria and liquid steel. Therefore, preventing the coarsening of the Y-rich nanoclusters during AM melting is very challenging. However, if the oxides could form in-situ during processing it would eliminate the need to mechanically alloy the powders.

The other approach is to fabricate the build in an oxidizing environment leading to the formation of these nanoclusters in-situ. The fundamental principle is similar to that of welding [15]–[17]. Welding in an oxidizing environment tends to produce a dispersion of oxide inclusions with an observed inclusion density of 10^{16} – 10^{17} m³ which are several tens of micrometers in diameter [15], [18]. However, careful control of the powder chemistry, oxidizing environments, heat input and cooling rate could result in smaller size and higher density resulting in the desired nanocluster formation. For instance, with a 1 kJmm^{-1} heat input the size of oxide particles range from 0.05–1.5 μm with a peak occurring at 0.3 μm ; however, when the heat input is increased to 8 kJmm^{-1} the distribution shifts to a broader distribution leading to the domination of coarse inclusion with the peak occurring at 0.5 μm [15]. Saeidi et al. [19], [20] and Springer et al. [21] have used this principle of inclusion formation and demonstrated that a dispersion of oxides can indeed form during SLM of austenitic stainless steels. They also demonstrated an improvement in the associated tensile properties at room temperature. However, the oxides that they reported were predominantly SiO_2 . While the ability to incorporate oxides in the build is indeed important, the impressive properties in mechanically milled ODS alloys stem from the nature of the oxide-matrix interface. The structure of these oxides were predominantly amorphous and they exhibited an incoherent and a sharp interface with the matrix [19]–[21]. However, recent work has shown that in the case of ball milled austenitic powders the primary deformation mechanism was dislocation looping in the case of the dispersoids which had a size $> 15 \text{ nm}$ while some cases of cutting was observed in dispersoids with a coherent interface with the austenitic matrix [4], [22]. In addition, the exact method of controlling the processing environment and the role of the processing atmosphere had not yet been discerned.

While the AM fabricated ODS steels did show an improvement in properties compared to its cast counter parts, this improvement could have resulted from the dramatic increases in strain hardening promoted by twinning and strain-induced plasticity mechanisms [23]. In addition, austenitic stainless steels fabricated using AM contains a significant amount of dislocations and stacking faults further improving the strain hardening during deformation [24]. The exact role of the particle sizes and the corresponding contribution to the strength increase and the stability of those particles during heat treatment needs to be evaluated. This necessitates a detailed study into the mechanisms operating during deformation of the ODS alloys fabricated with reactive metals such as Y. The objective of this study is to perform a preliminary investigation on the feasibility of producing Y based oxides in steels and to evaluate the influence of the processing atmosphere on the evolution of the microstructure.

2. EXPERIMENTAL PROCEDURE

A Y added variant of 316L stainless steel was obtained from Sandvik. The powders were gas atomized and had a size distribution of 45–125 μm . The composition of the as received powder is shown in Table 1. The builds were fabricated using the DMD-103D blown powder additive manufacturing system. The system was equipped with a 1 kW diode laser with a wavelength of 910 nm. Builds were fabricated with two

processing conditions, namely inert (99% Ar atmosphere) and under ambient atmosphere. The builds were fabricated using a laser power of 700 W with a travel speed of 700 mm/min and a powder mass flow rate of 5 grams per minute. Both builds were fabricated with the exact same processing conditions. The builds were then sectioned along the build direction (herein, the Z-direction) and mounted in conductive epoxy. The samples were polished using standard metallography techniques down to a defect free, mirror finish. Optical microscopy was performed using an Olympus microscope. Scanning electron microscopy (SEM) was performed using a JEOL 6500F field emission gun (FEG) SEM using a probe current of 4 nA and a voltage of 20 kV. Electron backscattered diffraction (EBSD) was performed to investigate the as-fabricated structure of the builds.

Table 1: Composition of the as-received powder in weight percent.

Fe	Cr	Ni	Mo	Si	Mn	Y	C	P	S
Bal	17.5	10.3	2.4	1.70	1.61	0.14	0.019	0.02	0.01

Following fabrication, tensile specimens were extracted for analysis. Standard SS-J3 tensile specimens [25] were extracted using wire EDM. Tensile tests were performed at room temperature, 200, 400 and 600°C in ambient atmosphere. Tensile testing was performed at a strain rate of 10^{-3} s^{-1} . The fracture samples were then mounted in conductive epoxy and polished using the standard metallographic techniques. To investigate the structure at the location of failure, EBSD was performed at those locations to identify the operating deformation mechanism using similar conditions described previously.

3. RESULTS AND DISCUSSION

3.1 Microstructure characterization

3.1.1 As-received powder

The structure of the as-received powder is presented in Figure 2. Figure 2 shows that the as-fabricated powder has a significantly refined grain structure with a fine dispersion of nano-oxides. No detailed TEM study was performed to understand if micro-segregation occurred during the atomization or if solidification occurred via a partitionless solidification mechanism as reported by Rieken et al. [11], [26]. The presence of a dispersion of oxides even in the atomized state seemed to indicate that oxidation of the powders did occur during the initial atomization stage as well. A more detailed characterization of the powder structure is necessary and will be performed in the future.

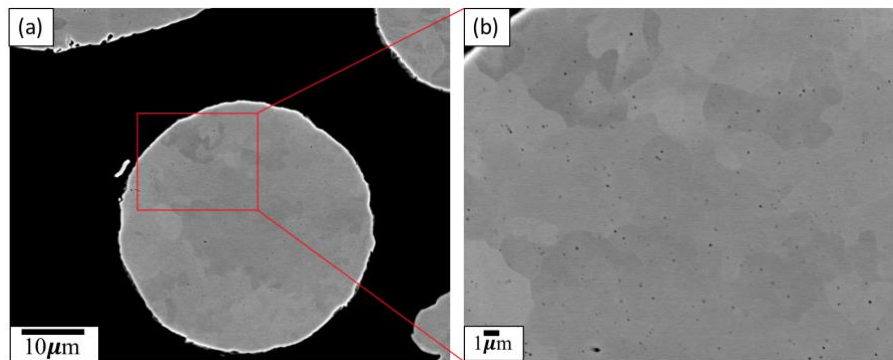


Figure 2: (a) Micrograph showing the structure and the presence of dispersoids in the as-fabricated powder (b) Figure 2(a) in higher magnification

3.1.2 As-fabricated structure

3.1.2.1 As-fabricated in ambient atmosphere

The structure of the samples in the as-fabricated condition is shown in Figure 3. Figure 3(a) shows the as-fabricated microstructure acquired using SEM. The inset in Figure 3(a) is a higher magnification area of the region marked. Figure 3(b) shows the size distribution of the oxide dispersoids which were extracted using ImageJ [27]. The data shows that while the oxides are dispersed uniformly; the number density is significantly lower compared to the number density obtained during mechanical alloying. In addition, the size of the precipitates is also significantly coarser compared to the mechanically alloyed counter parts [4], [22]. The lower number density is likely due to the loss of Y during processing. The chemical analysis of the samples showed significant loss in Y in the as-built state suggesting that it should be accounted for during the atomizing state. In addition, processing in atmosphere also resulted in an increased N pick up.

Table 2: Composition of the fabricated builds in weight percent

	Cr	Ni	Mo	Si	Mn	Y	C	N	O
Fabricated in atmosphere	17.38	10.3	2.28	1.70	1.55	0.06	0.016	0.0963	0.0330
Fabricated in Ar	17.39	10.3	2.28	1.70	1.48	0.07	0.012	0.0685	0.0149

To investigate the grain structure, EBSD was performed on the as-fabricated structure and the results are presented in Figure 4. Figure 4 shows the inverse pole figure of the as-fabricated sample and highlights an as-fabricated grain structure of $\sim 50 \mu\text{m}$. In addition, EBSD was performed at a higher magnification and is shown in Figure 4(b). The figure shows the presence of a body-centered cubic (BCC) phase, δ -ferrite, in the interdendritic regions which could be a consequence of the Ferrite-Austenite (FA) mode of solidification [28]–[30].

In contrast, the commercial ODS austenitic alloys have a grain size of $\sim 250 \text{ nm}$ and a number density of $10^{24-25} \text{ particles/m}^3$ [4], [5]. This work shows a mean particle size of $97 \pm 18 \text{ nm}$. However, no TEM analysis or small angle scattering was performed to identify if oxide dispersoids below the detectable SEM resolution could be observed. The measured size distribution is significantly finer compared to those reported to form during arc-based processes. These dispersoids have a strong correlation to the process parameters and it has been demonstrated that the size distribution changes as a function of heat input with lower heat inputs yielding a much finer distribution of the particles [15], [18]. Therefore, future experiments need to concentrate on evaluating the influence of processing conditions on the size distribution of the precipitates.

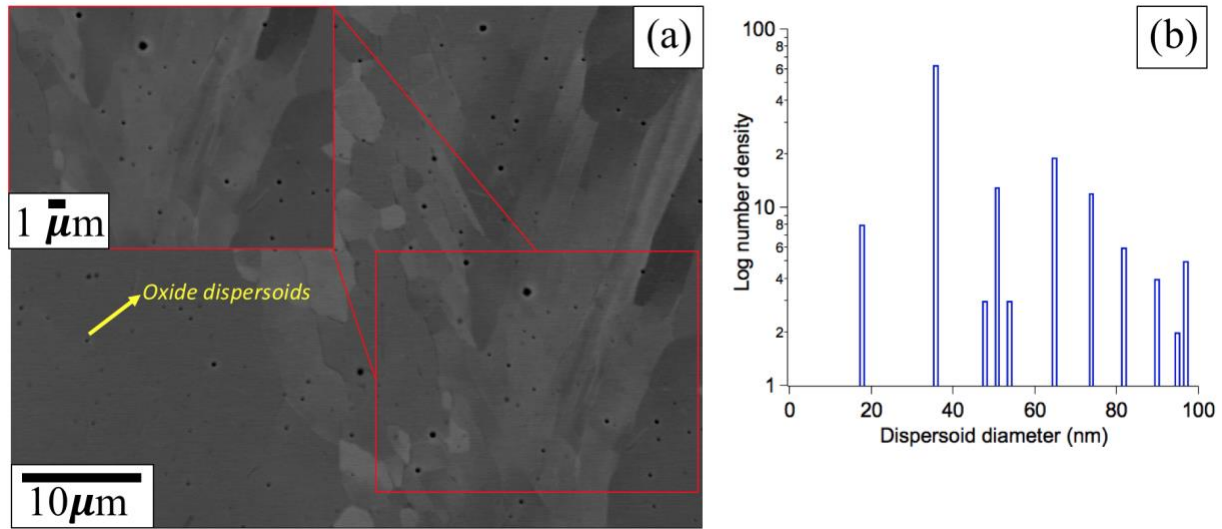


Figure 3: (a) Dispersoids (black contrast) embedded in the matrix and inset showing a magnified region in Figure 3(a). (b) Particle size distribution measured using ImageJ showing a peak at 30 nm with an average size of 97 nm.

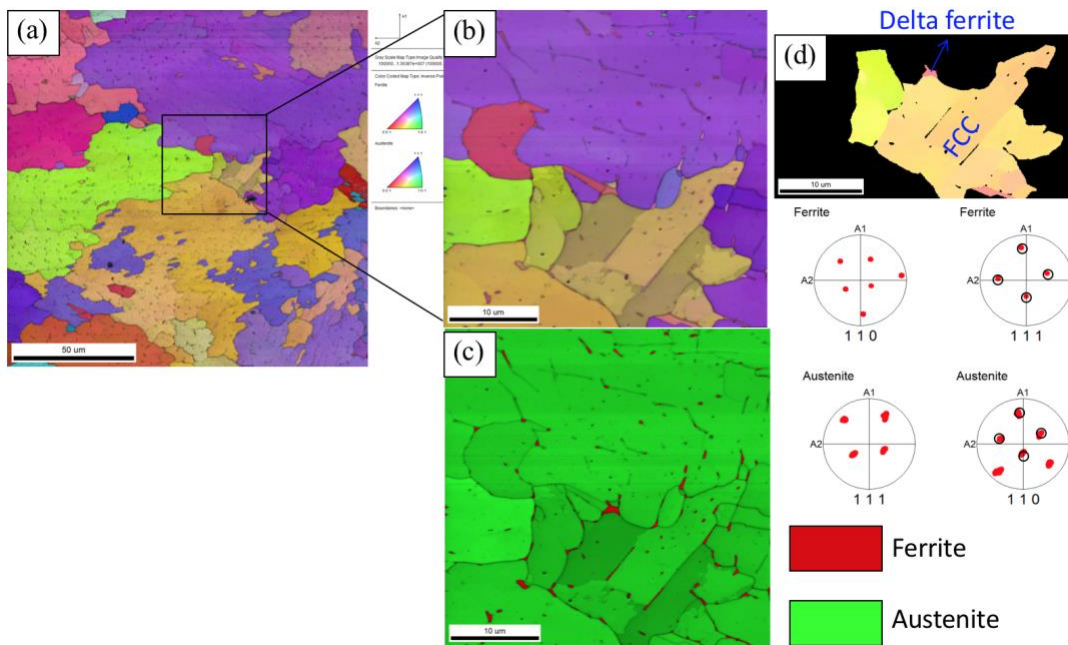


Figure 4: (a) Inverse pole figure (IPF) of the sample fabricated under atmosphere (b) Higher magnification IPF of the region marked in (a) (c) Phase map corresponding to (b) clearly showing the presence of δ ferrite formed as a consequence of solidification (d) Shows that δ -ferrite has an orientation relationship with the austenite phase

3.1.2.2 As-fabricated in inert atmosphere

The microstructure of the samples fabricated in the inert atmosphere is presented in Figure 5. Figure 5(a) shows the SEM micrographs of the samples fabricated in an inert atmosphere. The samples show relatively lower density of oxide dispersoids. Again, the size distribution of the precipitates is compared with those observed in the powder and the alloy which was fabricated in ambient atmosphere. The sample fabricated under inert atmosphere also shows similar losses in Y while the extent of N and O pick up in the sample is significantly lower. SEM-EBSD shows grains of similar sizes to those fabricated in the atmosphere. However, the major difference is the presence of higher amount of δ -ferrite in the samples fabricated in the inert atmosphere. This could be due to the lower N content in the steels fabricated in the inert environment which does not promote the formation of ferrite. Due to the lower oxygen content, the fraction of oxides in this sample is significantly lower compared to the sample fabricated in open atmosphere. However, the size distribution is finer compared to the samples fabricated in air with an average size of 79 ± 20 nm. The exact reason for this is still not known but it is hypothesized that in an O-lean atmosphere the precipitates are unable to coarsen and grow. Therefore, controlling the amount of O pickup in the build could also be an effective strategy to tune the dispersoids density as a function of processing conditions. To understand the difference in the O pickup in the samples, chemical analysis was performed and the results are shown in Figure 5(c). The figure clearly shows that the samples fabricated under Ar atmosphere have lower O and N pickup. However, the loss in Y content seems to be almost the same regardless of the processing conditions.

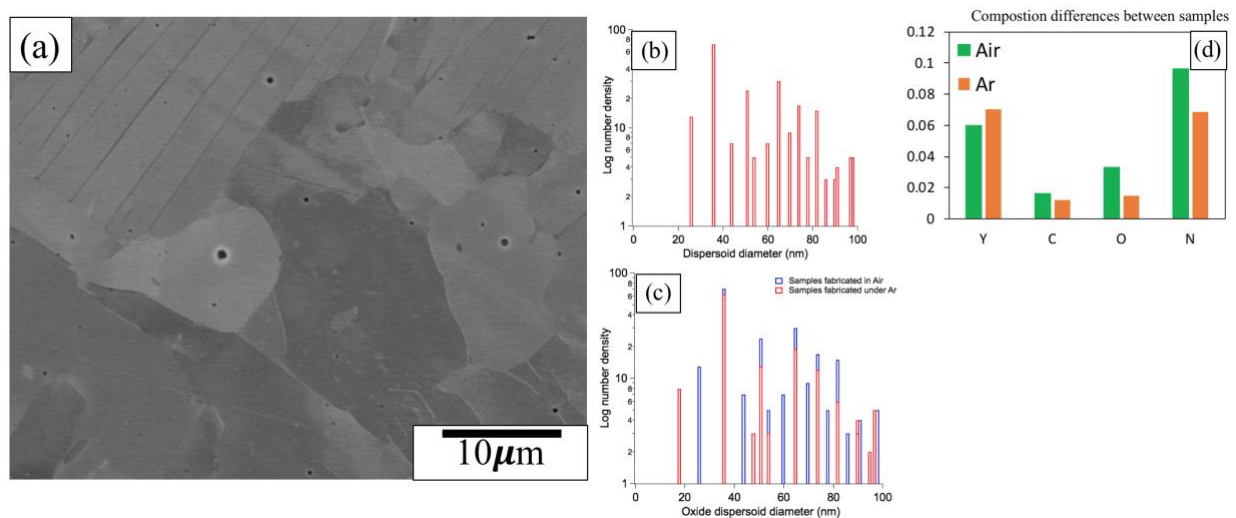


Figure 5: Structure of the as-fabricated sample (a) micrograph of the sample showing the presence of oxide nano-dispersoids (b) Histogram showing the size distribution of the oxide particles in the as-fabricated structure (c) Comparison between the size distributions of the samples fabricated in air and Ar (d) Showing the differences in N, O and Y between the two samples.

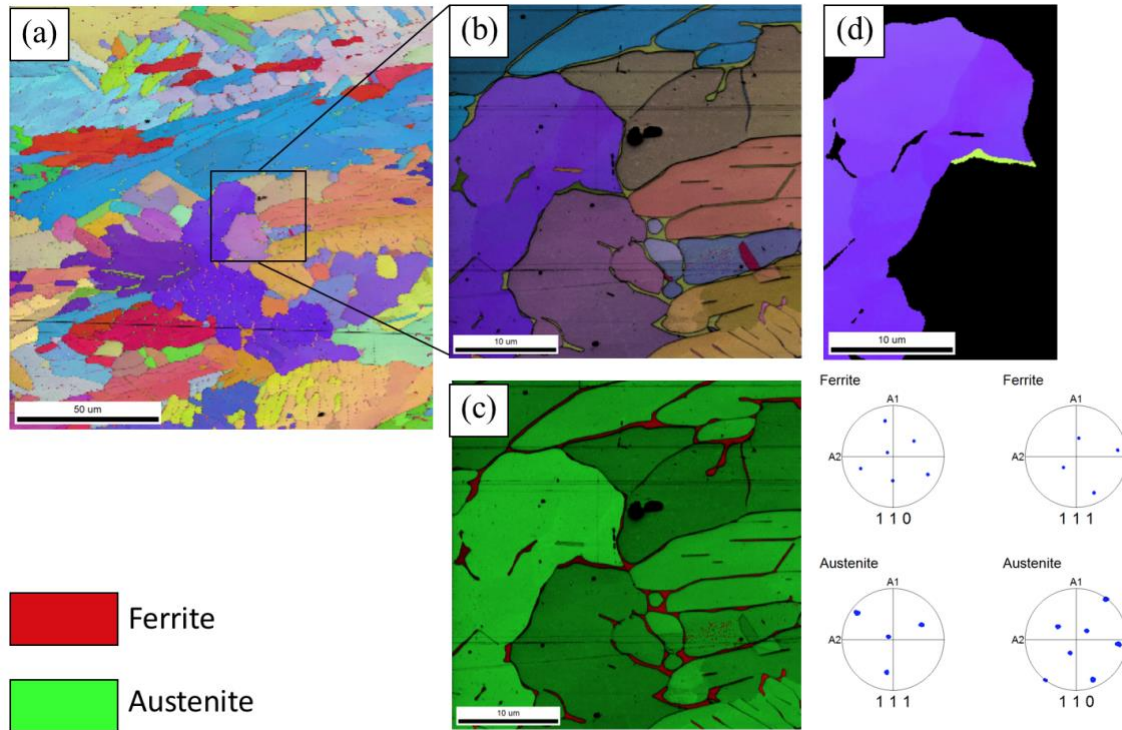


Figure 6: (a) Inverse pole figure (IPF) of the sample fabricated under Ar (b) Higher magnification IPF of the region marked in (a) (c) Phase map corresponding to (b) clearly showing the presence of δ ferrite formed as a consequence of solidification (d) Shows that δ -ferrite has an orientation relationship with the austenite phase

3.1.3 Mechanical behavior

The engineering stress-strain curves of the samples fabricated under inert and oxidizing atmosphere are presented in Figure 7. The data does not show a major difference in the room temperature and high temperature properties between the samples fabricated under Ar and without any shielding gases indicating that the oxide dispersoids do not contribute significantly to the overall strength of the alloy. The data also clearly shows a drop in the strength and ductility with increase in temperature. In order to compare the mechanical properties of the steel fabricated using AM with other ODS austenitic alloys a detailed survey of the literature was performed and the mechanical properties are summarized in Figure 8. The results show that while the ultimate tensile strength (UTS) of the alloys fabricated using AM followed very well with the results reported by Miao et al. (who also fabricated ODS alloys with similar compositions) the yield stress was significantly lower especially at higher temperatures. The mechanism of strength reduction with increase in temperature is attributed to the simultaneous activation of cross slip and climb. This is a consequence of the reduction in the barriers to overcome the self-diffusion coefficient. Miao et al. base this hypothesis on the pronounced increase in the fraction of screw dislocations during deformation at elevated temperatures. While this explains the drop-in strength, the resulting loss in ductility with increase in temperature is also not explained. Figure 8(b) shows the ductility of the 316L-ODS AM alloy with their wrought counterparts. The ductility was also surprisingly high compared to any ODS alloy fabricated in the literature and the samples fabricated both in air and Ar retained ductility.

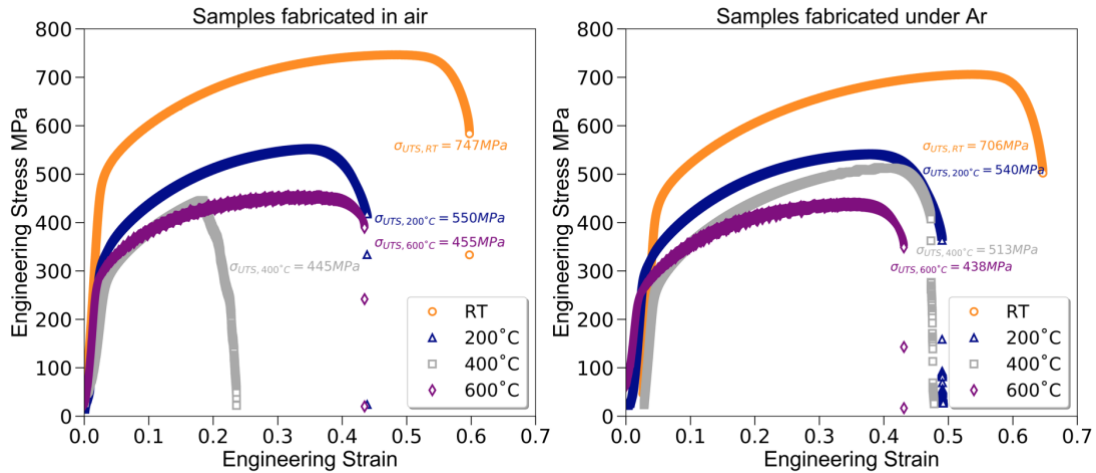


Figure 7: Engineering stress strain curves for the samples fabricated in air and in Ar.

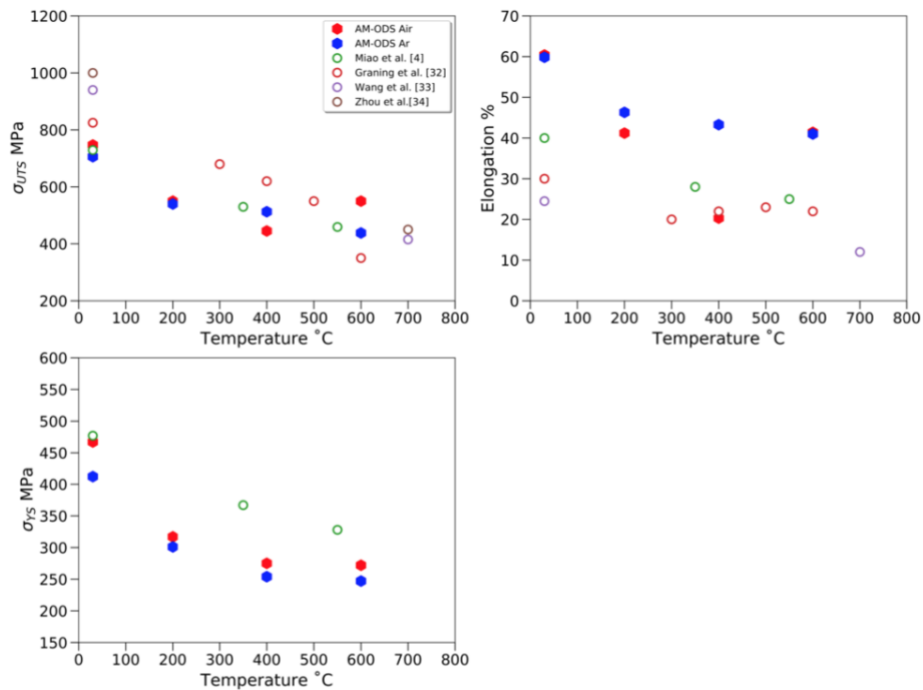


Figure 8: Comparison between the mechanical properties as a function of temperature for the AM ODS alloys vs wrought alloys [31]–[34].

On closer examination, Figure 8(c) shows a significant drop in yield strength of the material with increase in temperature while the UTS followed the trend of the 316L ODS alloy. The drop in both strength and ductility with increase in temperature is interesting since almost all the ODS alloys regardless of composition seemed to exhibit this trend.

Plasticity in austenitic steels is dominated by:

- Slip
- Twinning
- Strain induced martensite
- Dispersion hardening [23], [35]

While the roles of slip and dispersion hardening in improving the mechanical properties of austenitic stainless steels are well articulated in the literature, the role of twinning or extended stacking faults on the deformation behavior are not well understood [4], [5], [36]. Hence, to deconstruct the operating mechanisms EBSD in the deformed locations were performed to rationalize various mechanisms. The inverse pole figures are shown in Figure 9(a)-(d). The figures clearly show a decrease in the number of twins and the density of twins as the deformation temperature increases. At a temperature between 400°C and 600°C the number of twins decreases drastically, and the deformation is almost predominantly controlled via dislocation-based plasticity as discussed previously. The analysis clearly shows that at room temperature the deformation was predominantly controlled by twinning. However, as the temperature increased the mechanism switched to dislocation slip. This transition in micro mechanisms clearly explains the reasons for the drop in the ductility with increase in temperature.

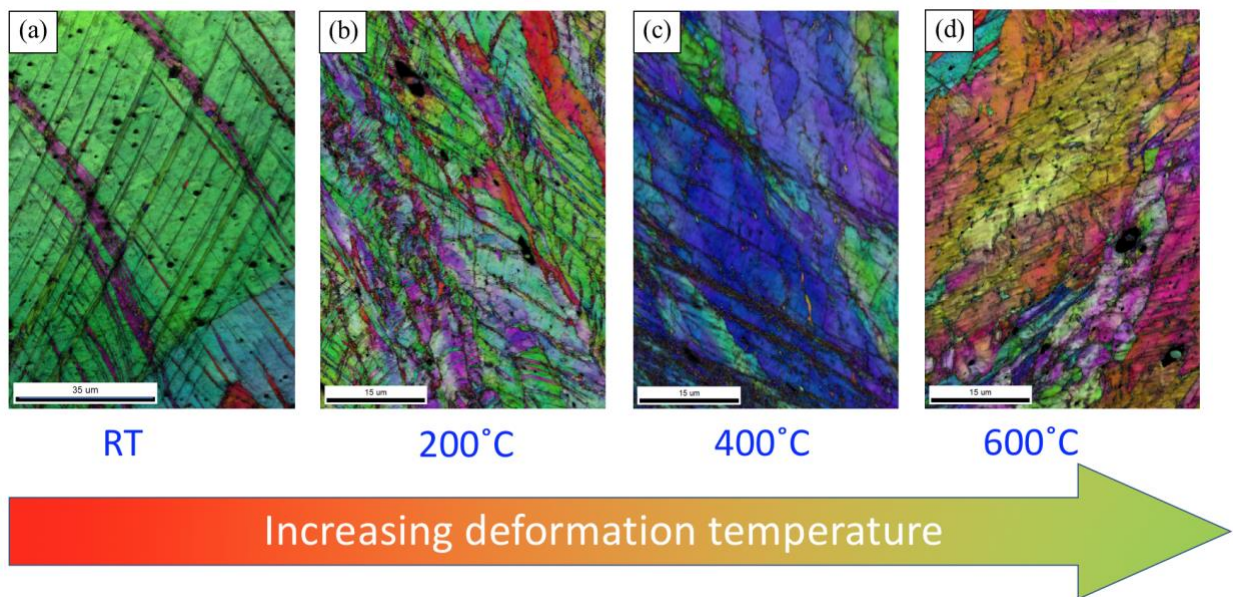


Figure 9: Inverse pole figure performed on the heads of the deformed specimens deformed at (a) RT (b) 200°C (c) 400°C and (d) 600°C note the decrease in the number of twins with increase in the deformation temperature.

4. SUMMARY AND CONCLUSIONS

Based on the preliminary investigation, it is shown that it is indeed possible to incorporate a dispersion of secondary dispersoids to incorporate dispersion strengthening in the builds. However, the composition of the feedstock powder needs to account for the losses in the reactive elements during processing. This loss of Y from the powder leads to the formation of a low volume fraction of the dispersoids ($\sim 2.8 \times 10^{18}/\text{m}^3$). In addition, the particle size distribution (measured from the SEM measurements) indicates that the particle sizes were close to 97 nm when fabricated in air and 79 nm when fabricated under Ar. However, it needs

to be pointed out that a detailed design of experiments was not performed to optimize the process parameters to produce a refined dispersion of the oxide phases. No post processing treatments were also evaluated. The alloys fabricated using AM showed strengths on par with the commercial ODS alloys at room temperature. While the alloys retained their strength at RT, at higher temperatures the yield strength rapidly decreased in comparison to other wrought ODS alloys. In addition, the ductility of the alloys also decreased with an increase in temperature. Post deformation characterization showed that this behavior was primarily due to a plasticity mechanism which was governed by twinning. Further optimization in terms of composition of the feedstock, processing atmosphere and processing parameters need to be performed before any ODS material with significant precipitate strengthening can be produced.

5. REFERENCES

- [1] S. J. Zinkle and G. S. Was, "Materials challenges in nuclear energy," *Acta Mater.*, 2013.
- [2] G. R. Odette, M. J. Alinger, and B. D. Wirth, "Recent developments in irradiation-resistant steels," *Annu. Rev. Mater. Res.*, vol. 38, pp. 471–503, 2008.
- [3] S. J. Zinkle and L. L. Snead, "Designing radiation resistance in materials for fusion energy*," *Annu. Rev. Mater. Res.*, vol. 44, pp. 241–267, 2014.
- [4] Y. Miao *et al.*, "The interfacial orientation relationship of oxide nanoparticles in a hafnium-containing oxide dispersion-strengthened austenitic stainless steel," *Mater. Charact.*, vol. 101, pp. 136–143, 2015.
- [5] Y. Miao *et al.*, "On the microstructure and strengthening mechanism in oxide dispersion-strengthened 316 steel: A coordinated electron microscopy, atom probe tomography and in situ synchrotron tensile investigation," *Mater. Sci. Eng. A*, vol. 639, pp. 585–596, 2015.
- [6] S. Ukai, "Oxide dispersion strengthened steels," in *Comprehensive Nuclear Materials*, 2012.
- [7] F. Bergner *et al.*, "Alternative Fabrication Routes toward Oxide-Dispersion-Strengthened Steels and Model Alloys," *Metall. Mater. Trans. A Phys. Metall. Mater. Sci.*, 2016.
- [8] S. Ukai *et al.*, "Tube manufacturing and characterization of oxide dispersion strengthened ferritic steels," *J. Nucl. Mater.*, 2000.
- [9] M. J. Aziz, "Model for solute redistribution during rapid solidification," *J. Appl. Phys.*, 1982.
- [10] J. R. Rieken *et al.*, "Atomized precursor alloy powder for oxide dispersion strengthened ferritic stainless steel," *Adv. Powder Metall. Part. Mater.*, 2008.
- [11] J. R. Rieken and I. E. Anderson, "Gas atomized precursor alloy powder for oxide dispersion strengthened ferritic stainless steel," *Mater. Sci. Eng.*, 2011.
- [12] R. L. Terpstra, I. E. Anderson, F. Laabs, and J. R. Rieken, "Simplified powder processing of oxide dispersion stainless steel," *Adv. Powder Metall. Part. Mater.*, 2006.
- [13] T. Boegelein, E. Louvis, K. Dawson, G. J. Tatlock, and A. R. Jones, "Characterisation of a complex thin walled structure fabricated by selective laser melting using a ferritic oxide dispersion strengthened steel," *Mater. Charact.*, vol. 112, pp. 30–40, 2016.
- [14] T. Boegelein, S. N. Dryepondt, A. Pandey, K. Dawson, and G. J. Tatlock, "Mechanical response and deformation mechanisms of ferritic oxide dispersion strengthened steel structures produced by selective laser melting," *Acta Mater.*, 2015.
- [15] O. Grong, "Metallurgical Modelling of Welding," *Inst. Mater. 1 Carlt. House Terrace, London, SW 1 Y 5 DB, UK, 1997. 605*, 1997.

- [16] S. S. Babu and S. A. David, "Inclusion Formation and Microstructure Evolution in Low Alloy Steel Welds," *ISIJ Int.*, vol. 42, no. 12, pp. 1344–1353, 2002.
- [17] K. C. Hsieh, S. S. Babu, J. M. Vitek, and S. A. David, "Calculation of inclusion formation in low-alloy-steel welds," *Mater. Sci. Eng. A*, vol. 215, no. 1, pp. 84–91, 1996.
- [18] Grong and H. R. Shercliff, "Microstructural modelling in metals processing," *Prog. Mater. Sci.*, 2001.
- [19] K. Saeidi, L. Kvetková, F. Lofaj, and Z. Shen, "Austenitic stainless steel strengthened by the in situ formation of oxide nanoinclusions," *RSC Adv.*, 2015.
- [20] K. Saeidi, "Stainless steels fabricated by laser melting: Scaled-down structural hierarchies and microstructural heterogeneities," 2016.
- [21] H. Springer *et al.*, "Efficient additive manufacturing production of oxide-and nitride-dispersion-strengthened materials through atmospheric reactions in liquid metal deposition," *Mater. Des.*, vol. 111, pp. 60–69, 2016.
- [22] Y. Miao *et al.*, "On the microstructure and strengthening mechanism in oxide dispersion-strengthened 316 steel: A coordinated electron microscopy, atom probe tomography and in situ synchrotron tensile investigation," *Mater. Sci. Eng. A*, 2015.
- [23] G. M. De Bellefon and J. C. Van Duysen, "Tailoring plasticity of austenitic stainless steels for nuclear applications: Review of mechanisms controlling plasticity of austenitic steels below 400°C," *Journal of Nuclear Materials*. 2016.
- [24] Y. M. Wang *et al.*, "Additively manufactured hierarchical stainless steels with high strength and ductility," *Nat. Mater.*, 2017.
- [25] M. N. Gussev, R. H. Howard, K. A. Terrani, and K. G. Field, "Sub-size tensile specimen design for in-reactor irradiation and post-irradiation testing," *Nucl. Eng. Des.*, vol. 320, pp. 298–308, Aug. 2017.
- [26] J. R. Rieken, "Gas atomized precursor alloy powder for oxide dispersion strengthened ferritic stainless steel," 2011.
- [27] C. A. Schneider, W. S. Rasband, and K. W. Eliceiri, "NIH Image to ImageJ: 25 years of image analysis," *Nature Methods*. 2012.
- [28] J. C. Lippold and D. J. Kotecki, "Welding Metallurgy and Weldability of Stainless Steels," ... *Metallurgy and Weldability of Stainless* p. pp 1, 141-145, 2005.
- [29] J. A. Siefert and S. A. David, "Weldability and weld performance of candidate austenitic alloys for advanced ultrasupercritical fossil power plants," *Sci. Technol. Weld. Join.*, vol. 19, no. 4, pp. 271–294, 2014.
- [30] J. M. Vitek, A. Dasgupta, and S. A. David, "Microstructural modification of austenitic stainless steels by rapid solidification," *Metall. Trans. A*, vol. 14, no. 9, pp. 1833–1841, 1983.
- [31] L. Raman, K. Gothandapani, and B. S. Murty, "Austenitic oxide dispersion strengthened steels: A review," *Defence Science Journal*. 2016.
- [32] T. Gräning, M. Rieth, J. Hoffmann, and A. Möslang, "Production, microstructure and mechanical properties of two different austenitic ODS steels," *J. Nucl. Mater.*, 2017.
- [33] M. Wang, Z. Zhou, H. Sun, H. Hu, and S. Li, "Microstructural observation and tensile properties of ODS-304 austenitic steel," *Mater. Sci. Eng. A*, 2013.
- [34] Z. Zhou, S. Yang, W. Chen, L. Liao, and Y. Xu, "Processing and characterization of a hiped

- oxide dispersion strengthened austenitic steel,” in *Journal of Nuclear Materials*, 2012.
- [35] P. Susila, D. Sturm, M. Heilmaier, B. S. Murty, and V. Subramanya Sarma, “Microstructural studies on nanocrystalline oxide dispersion strengthened austenitic (Fe-18Cr-8Ni-2W-0.25Y₂O₃) alloy synthesized by high energy ball milling and vacuum hot pressing,” in *Journal of Materials Science*, 2010.
- [36] Y. Miao *et al.*, “Load-partitioning in an oxide dispersion-strengthened 310 steel at elevated temperatures,” *Mater. Des.*, 2016.